Page Proof Instructions and Queries

Greetings, and thank you for publishing with SAGE. We have prepared this page for your review. Please respond to each of the below queries by digitally marking this PDF using Adobe Reader (free at https://get.adobe.com/reader).

Please use *only* the circled tools to indicate your requests and responses, as edits via other tools/methods are not compatible with our software. To ask a question or request a formatting change (such as italics), please click the ⊕ tool and then choose "Text Callout." To access the necessary tools, choose "Comment" from the right-side menu.
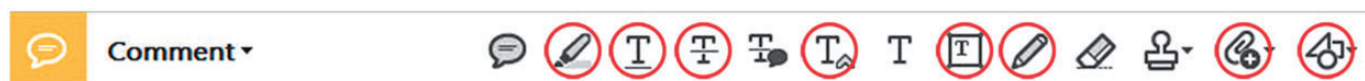
No.	Query
	Please confirm that all author information, including names, affiliations, sequence, and contact details, is correct.
	Please review the entire document for typographical errors, mathematical errors, and any other necessary corrections; check headings, tables, and figures.
	Please confirm that the Funding and Conflict of Interest statements are accurate.
	Please ensure that you have obtained and enclosed all necessary permissions for the reproduction of artistic works, (e.g. illustrations, photographs, charts, maps, other visual material, etc.) not owned by yourself. Please refer to your publishing agreement for further information.
	Please note that this proof represents your final opportunity to review your article prior to publication, so please do send all of your changes now.
AQ: 1	Please provide further details in ref. 4.
AQ: 2	Please provide the accessed date for the URL in ref. 20.

A novelty technique for the fabrication of biomedical optics phantoms with cyst-mimicking inclusions

PA Pardini, JA Pomarico and DI Iriarte

Abstract

The construction of standardised phantoms for biomedical optics experiments is still a developing research field. Particularly, the application of diffusive optics techniques to tissues with low or non-scattering heterogeneities, such as cysts, where the diffuse approximation does not apply, has been studied during the last years. The reported phantoms for mimicking cysts have inclusions that consist of hollow cylinders filled with low or non-scattering fluids, being thus more representative of a 2D geometry rather than a 3D geometry. We present here an innovative proposal, to our knowledge not reported before, for the manufacture of solid diffusive phantoms with spherical, liquid inclusions, with low or non-scattering properties, intended to reproduce cysts. To this end, we used the inverse spherification technique from the molecular gastronomy. The constructed phantoms were optically characterised by two approaches, namely whole field continuous wave transmittance imaging and time-resolved experiments, both in the near infrared at $\lambda = 785$ nm. After optical characterisation, the phantoms were also dissected, showing that the inclusions remained in place and preserved their shape after the whole fabrication process. Some results were also validated by Monte Carlo simulations.

Introduction

Light propagation in turbid media, such as biological tissue, has become increasingly interesting during the last two decades, and special attention has been paid to its potential application for the study and characterisation of mammary tissue, joints and brain. Thus, this technique constitutes an important, non-invasive tool for the diagnosis of some diseases and their treatment.

The propagation of light in diffusive media is generally described by the diffusive approximation (DA), which corresponds to the lower order of the Boltzmann transport equation (BTE).[1] Even when this approximation is capable of reproducing accurate results in many practical situations, it is not valid on the low and non-scattering regime, which is the case for cysts, cerebrospinal fluid and synovial fluid in joints.[2–5] To overcome these limitations, different approaches have been proposed based on the BTE, Monte Carlo (MC) simulations, finite element methods, or higher-order approximations following the diffuse approximation.[2,3,6–8]

Whichever the case, to evaluate their applicability to real tissue, these approaches need to be contrasted with experiments performed on phantoms, which are tissue-like constructions of known and controlled geometry and composition, commonly used in the development and characterisation of imaging systems and reconstruction algorithms. These phantoms can be either solid or liquid. The solid phantoms are frequently made of resins, plastics or gels, while liquid ones are fabricated of distilled water mixed with some scattering agent, such as Intralipid® or milk, and an absorbent agent, generally pre-diluted ink.[9–15]

From a pure academic point of view, modelling light propagation in biological tissues containing low or non-scattering heterogeneities is important to study

Instituto de Física Arroyo Seco – IFAS (UNCPBA) and CIFICEN (UNCPBA-CICPBA-CONICET), Pinto, Tandil, Argentina

Corresponding author:
PA Pardini, Instituto de Física Arroyo Seco – IFAS (UNCPBA) and CIFICEN (UNCPBA-CICPBA-CONICET), Pinto 399, Tandil 7000, Argentina.
Email: ppardini@exa.unicen.edu.ar

their influence on the solution of inverse problems, to include all the possible clinical situations, and when considering cysts, joints, synovial fluid, void regions on stomach, oesophagus, intestine and bladder, which have low or non-scattering properties.[2,6,16–18] Additionally, there is particular local interest, related to the parasite *Echinococcus granulos*, that generates hydatid cysts. These parasites can be found in almost every country, but are hyperendemic in South America, particularly in Argentina where it constitutes the principal zoonotic disease, as is also the case in some countries of Asia and Africa, while it is endemic in the rest of the world.[19] The development of drugs against this disease requires infecting small animals, which are then sacrificed to evaluate the cyst reduction due to the action of the drug. Therefore, to avoid or reduce the number of sacrificed animals, it is of high importance to rely on imaging techniques to localise and characterise cyst-like inhomogeneities, allowing *in vivo* evaluation of the action of different antiparasitic drugs. Cyst emulating phantoms are thus important for the development of these imaging techniques.

In this work, we present a novel procedure for constructing solid phantoms based on agarose, containing spherical liquid inclusions, with low or non-scattering properties. Inclusions were elaborated using a technique from the area of *molecular gastronomy* called inverse spherification,[20] to our knowledge never reported before for the construction of phantoms. The whole procedure is simple, fast and of low cost, and it is well suited to be used in conjunction with diffuse optical imaging systems.

The paper is organised as follows: in the *Phantom fabrication* section, we describe the procedure used for the phantom manufacturing. In the next two sections, we describe the methods followed for their evaluation and we discuss the results obtained. Finally, a summary of the main conclusions is presented.

Phantom fabrication

Manufacturing the phantoms described here requires at least two steps, namely, (1) the preparation of the liquid inclusion, and (2) the elaboration of the solid host, which we chose to be made of agarose, containing the liquid cyst-like spherical inclusion. Both steps are described in detail below.

Optical properties of turbid media are given by the reduced scattering coefficient (μ'_s), which is the inverse of the transport mean free path, and the absorption coefficient (μ_a), which is the reciprocal of the mean path travelled by a photon before it is absorbed. For obtaining the desired ones of both, host and inclusions, we used a mixture of distilled water, whole milk (3% fat) as the scattering agent and ink as the absorber (Powertec® HP PIG4844 black http://www8.hp.com/cl/es/products/oas/product-detail.html?oid=12882). For example, by taking proportions $35:65:3 \times 10^{-5}$ (milk:water:ink) resulted in $\mu'_s \approx 10\,cm^{-1}$ and $\mu_a \approx 0$.

$1\,cm^{-1}$, which are typical values for healthy living tissue[21] and which were used in this work for the host. Additionally, since we are interested in inclusions with low or non-scattering and low absorption coefficients, these proportions were conveniently varied. For this work, we used inclusions made from three different mixtures, namely (*A*), containing only distilled water, (*B*) with proportions 10:90:0 (milk:water:ink) and (*C*) $35:65:6 \times 10^{-5}$ (milk:water:ink). Type (*A*) and (*B*) inclusions are intended to simulate cysts with non-scattering and low scattering, respectively, while type (*C*) inclusions represent tumour-like lesions, with the approximate host scattering and increased absorption.

Since type (*A*) inclusions consisted only of distilled water, their reduced scattering coefficient can be taken as $\mu'_s(A) = 0$ and the absorption coefficient can be taken from Taroni et al.,[22] being $\mu_a^{(A)} = 0.02\,cm^{-1}$. For inclusions of type (*C*), which were diffusive but containing double the ink proportion than the host, the optical properties were measured from a Time-Resolved (TR) diffuse transmittance experiment. The TR setup and fitting procedure for obtaining the optical properties of a homogeneous medium are explained in detail in the Characterisation of the phantoms section. Using this approach, the optical properties measured for type (*C*) inclusions were $\mu'_s(C) = 10 \pm 1\,cm^{-1}$ and $\mu_a^{(C)} = 0.2 \pm 0.02\,cm^{-1}$. The optical properties of type (*B*) inclusions, however, could not be measured directly from diffusion experiments because of their low scattering which precluded the use of the diffusion model for obtaining them. Instead, we inferred these optical properties by extrapolation of calibration curves of μ'_s vs milk proportion, assuming that linearity held for low milk proportions. The resulting optical properties were thus $\mu'_s(B) = 2.5 \pm 0.3\,cm^{-1}$ and $\mu_a^{(B)} = 0.15 \pm 0.02\,cm^{-1}$. Although these values may not be very precise, it should be noted that it is not the main goal of this contribution to retrieve the actual optical properties of the inclusions, but to demonstrate that the proposed fabrication method produces phantoms of practical relevance.

1. Fabrication of the inclusion: the inverse spherification technique from the molecular gastronomy

The spherical inclusions with a thin gel membrane and liquid inside were fabricated with the inverse spherification technique from the so-called molecular gastronomy, and then introduced into the host of agarose, while this last one still remained liquid.

The components required were sodium alginate, a natural gelling agent extracted from brown algae, and calcium lactate, which is a calcium salt.

The inverse spherification consisted of the following three steps:[20]

(i) First, a solution (S1) for the inclusion was prepared and mixed with 1.5% in weight of calcium lactate.

(ii) A bath of distilled water with 0.4% in weight of sodium alginate (solution S2) was prepared and left to rest for about thirty minutes.

(iii) In this last step, the spheres were formed by selecting a desirable volume for the inclusions taken from solution S1 (for example using a syringe) and introducing it, all at once, into the bath of solution S2. After about 2 min, a thin spherical shell formed around the volume of solution S1, leaving it trapped inside, which constituted the desired inclusion. Then inclusions could be taken out from the bath and used in the phantom.

As an example, some spheres obtained using this method are shown in Figure 1: Figure 1(a) shows two
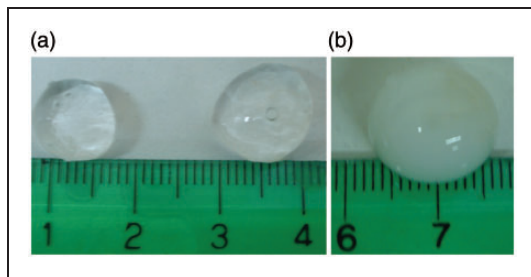
type (*A*) inclusions and Figure 1(b) is the picture of a single inclusion from type (*B*). Note that type (*A*) inclusions were completely transparent, since they contained no scattering agent, while the inclusion of type (*B*) was not, due to the milk inside it.

2. Host fabrication and phantom assembly

The host where the inhomogeneities were to be introduced consisted of a block made of the mix of distilled water, milk and ink in the proportions $35{:}65{:}3 \times 10^{-5}$ (milk:water:ink), as already described, and 1.5% in weight of agarose (Biodynamics SRL; http://www.biodynamics.com.ar).

The final assembly of the whole phantom was reached through the following steps (please refer to Figure 2(a) for the geometrical details):

1. The desired solution with optical properties for the host was mixed with the agarose, and heated up to 90°C while being stirred carefully, so that the agarose was completely dissolved. Then, this hot solution was poured into a mould with the shape of the phantom up to the desired depth of the inclusions (coordinate z, indicated in Table 1).

2. While the solution with agarose was still liquid (~45°C), the inclusions were placed on its surface at the desired (x, y) positions, as indicated in Table 1.

Figure 1. Examples of inclusions obtained by the inverse spherification technique with (a) water and (b) water:milk (3:0.1). The volumes of the solution inside the inclusions were chosen to obtain the desired diameters.
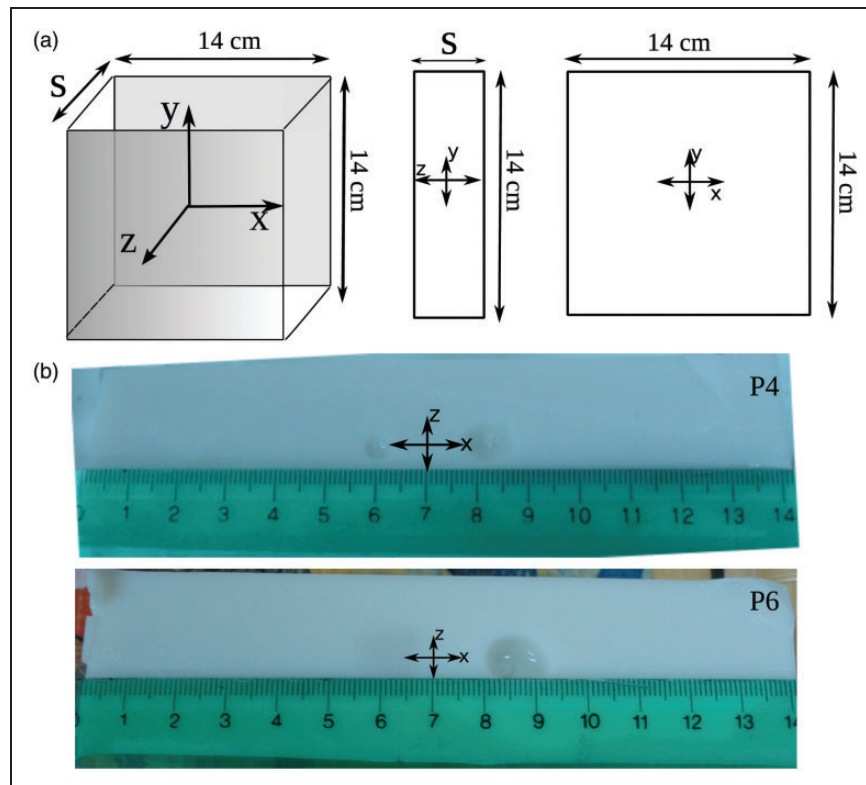

Figure 2. Phantom outline (a) showing the geometry used for all experiments and cut of phantoms P4 and P6 (b).

Table 1. Characteristics of the six constructed phantoms, identifying the number of inclusions, their type and location relative to the centre of the phantom.

Phantom	No. of inclusions	Diameter (cm)	Position (x,y,z) (cm)	Inclusion type
P1	1	Φ_1: 1.0	1: (−0.3, −0.3, 0)	**A**
P2	1	Φ_1: 1.0	1: (−0.2, 0, 0)	**B**
P3	2	Φ_1: 1.0	1: (−1.2, 0.2, −0.5)	**A**
		Φ_2: 1.0	2: (1.7, 0.2, −0.5)	**A**
P4	2	Φ_1: 1.0	1: (−1.2, 0, −0.3)	**A**
		Φ_2: 0.6	2: (1, 0, −0.2)	**A**
P5	2	Φ_1: 1.0	1: (−0.2, −0.5, 0)	**A**
		Φ_2: 0.6	2: (1.2, −0.5, 0)	**A**
P6	2	Φ_1: 1.0	1: (−0,8, 0.2, −0.2)	**C**
		Φ_2: 1.0	2: (1.4, 0.2, −0.2)	**A**

Note: Refer to Figure 2(a) for geometry.

3. After some minutes, when the exposed surface of the bulk cooled down and started to solidify, the rest of the agarose solution was poured into the form, leaving the inclusions trapped inside the agarose bulk.

After complete cooling down to room temperature, the phantom was ready and was taken out from the mould. The cooling down process took up to a couple of hours depending on the total volume, and could be accelerated by placing the phantom in a refrigerator.

Characterisation of the phantoms

General considerations

To determine if the phantoms constructed as proposed above are suitable to be used in biomedical optics experiments, we describe in this section some different procedures for their optical characterisation. The first one consists of whole field continuous wave (CW) transmittance imaging, allowing a rapid location of the inclusions. Next, TR experiments are presented which account for the low or non-scattering properties of the inclusions.

In all experiments, the light source was a ps semiconductor laser (Becker & Hickl – BHLP700, http://www.becker-hickl.com/pdf/redlaser3.pdf), operating at $\lambda = 785$ nm and 50 MHz, producing 70 ps pulses at an average power of 6 mW. Though this source was used specifically for the TR experiments, it was also suitable for performing CW imaging, since the integration time of the camera ($\sim$1 s) was long enough to include many pulses. Light from the laser was properly launched into a 600 µm core diameter optical fiber, with numerical aperture NA = 0.39 which distal end illuminated the entrance face of the phantom.
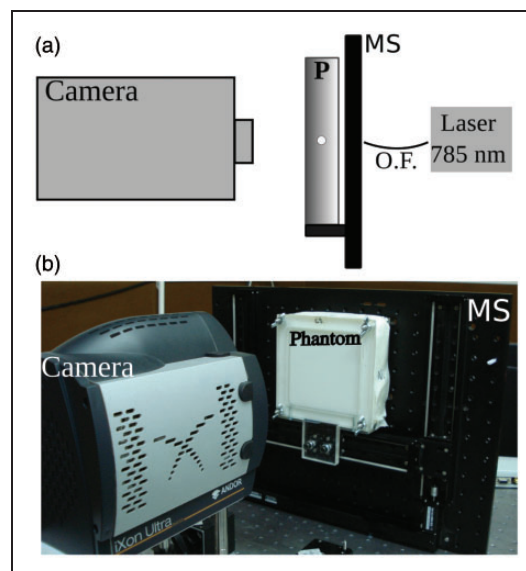

Figure 3. Set-up for *continuous wave transmittance (*CW) experiments: (a) schema and (b) photography of the actual experiment (P: phantom, MS: movable stage, O.F.: optical fibre, with collimator).

With reference to the geometry presented in Figure 2(a), six phantoms with different inclusions were constructed accordingly with the details given in Table 1. In all cases, the diameters of the inclusions were measured previous to embedding them in the agarose host.

In Figure 2(b) are shown, as an example, cuts of phantoms P4 and P6 through the plane containing the diameters of the inclusions. These photographs demonstrated that both the size and the shape of the inclusions were preserved when they were embedded in agarose. This is a mandatory condition if calibrated inclusions are to be introduced into the host.

CW imaging

For this experiment, we used the set-up shown in Figure 3. The whole phantom, a slab of lateral dimensions 14 cm × 14 cm and thickness $s = 4$ cm (see Figure 2(a)), was mounted inside an acrylic frame which was attached to a two-axis motorised translation stage with micron resolution (Zaber Technologies TGLSM200A200A), shown as MS in Figure 3. This allowed precise and repeatable 2D positioning of the phantom in the (x, y) plane, parallel to the surface imaged by the camera. Light emerging from the optical fibre impinged on one face of the phantom, at the point $(x, y, z) = (0, 0, -s/2)$. The diffuse transmitted light emerging at the opposite face was imaged by an EMCCD camera (Andor iXon Ultra 987 http://www.andor.com/scientific-cameras/ixon-emccd-camera-series/ixon-ultra-897), resulting in an image $I(x, y, s/2)$. The imaged region of the phantom surface had an approximate area of 6.3×6.3 cm^2. Images were analysed following the method described in the work by Carbone

et al.[23] Briefly, in that contribution, images of the medium containing the inclusions were normalised by dividing them, pixel by pixel, by a homogeneous background (ideally the same medium imaged but without inhomogeneities). This procedure emphasised the subtle intensity variations which occured due to the inclusions, making evident their presence. Clearly, in practical cases, the inhomogeneities cannot be removed to produce the background. Instead, we proceeded by acquiring several images of the phantom, $I_j(x, y)$. Between different images, the phantom was translated parallel to its surface. By averaging these images, the influence of blurring of the inclusions was minimised, and this averaged image was used as the normalisation background. Thus, the resulting normalised image, $I_j^N(x, y)$, of the medium is given by

$$I_j^N(x, y) = \frac{I_j(x, y)}{\frac{1}{M} \sum_{j=1}^{M} I_j(x, y)} \tag{1}$$

being M the total number of images. Note that in the regions far from the inclusions, each image was almost equal to the average normalisation background and as a consequence $I_j^N(x, y) \to 1$ in those regions.

We applied this procedure by moving the phantoms with the help of the motorised stage in x and y directions, in steps of 0.5 cm, obtaining a grid consisting of 81 images, scanning the complete area of the phantom. The whole set of measurements, took about 5 min.

In order to quantify the contrast of these normalised images, we took from each image a horizontal profile $P(x)$ along the x axis, through the diameter of the inclusions and we defined the contrast in percentage, relative to the background by

$$C_{CW}(x) = [P(x) - 1] \times 100 \tag{2}$$

Note that this percentage contrast was calculated using the value one as a reference, since it was the value of $P(x)$ far from the inclusion. This definition of the contrast also allowed comparison to the TR measurements, as will be clear later. With this definition of the contrast, regions of the phantom without inhomogeneities will have $C_{CW}(x) = 0$, while regions where the inhomogeneities were detected produced contrasts $C_{CW}(x) > 0$ or $C_{CW}(x) < 0$ for inhomogeneities less absorbing and more absorbing than the host, respectively.

Additionally, a MC simulation for the phantom P1 was performed to validate the result from the CW imaging. The MC simulation used a self-developed code which is explained in detail in Carbone et al.[24] To overcome the drawback of the intrinsic time-consuming nature of MC simulations, for simulations in turbid media containing inhomogeneities, a very fast MC algorithm was used that performs computing on GPU instead of using the CPU, and is based on Compute Unified Device Architecture (CUDA). Due to the parallel processing capability of GPU, and depending on the graphics card used, calculation times can be reduced by up to several orders of magnitude. The GPU used was a GForce® 8600GT Nvidia (Santa Clara, California, USA) graphic card installed in a personal computer with a Core 2 Duo, 2.66-GHz CPU.

The code allows a flat geometry configuration containing spherical inhomogeneities. Photons bundles were launched normal to the entrance face of a slab of thickness S at the origin and the inclusion was located at 2 cm depth and at 2 cm from the laser reproducing the configuration of Figure 3, and they were tracked until they were either absorbed, or exited the medium at the opposite face of the phantom within a defined detection area. Fresnel reflections at the entrance were considered. However, taking into account Fresnel reflections at the bulk–inclusion boundary can be very time consuming, since when a photon reaches this interface, the incidence angle must be evaluated, which in turn depends on the chosen geometry for the inclusion. Instead, in this proposal, these reflections were considered according to the suggestion of Ripoll and Nieto-Vesperinas,[25] in which the actual reduced scattering coefficient of the inclusion was replaced by an effective one defined by $\mu'(eff) = n_{rel}^2 \mu'_s$, being $n_{rel} = n_{bulk}/n_{inclusion}$. Diffusely transmitted photons were collected on a grid at the emerging surface emulating the CCD detectors. The optical properties of the turbid bulk were taken from those used for the phantom experiments. The scattering coefficient of the type (A) inclusion was considered null and its absorption coefficient, $\mu_a = 0.02$ cm^{-1}, was taken from the absorption of water at $\lambda = 785$ nm.[22] Two diffuse transmittance images were generated, namely one with the inclusion inside the turbid medium and one without it. This last one provided the normalisation background. The procedure followed for analysing the image was the same as for the experiments.

Time-resolved measurements

For a more detailed characterisation of the phantoms, we performed measurements in TR transmittance geometry. The experimental set-up is shown in Figure 4. The ps laser source illuminated the phantom via the optical fiber as described previously, and the light emerging at the opposite face of the phantom was collected by a 1/8 inch (3.175 mm) diameter optical fiber bundle. This was mounted coaxially to the source fiber, and its distal end was connected to a photomultiplier (Becker & Hickl PCM-100-20 http://www.becker-hickl.de/pdf/dbpmc.pdf, shown as PMT in Figure 4). Its electrical output was connected to a Time-Correlated Single-Photon Counting board (Becker & Hickl SPC 130 http://www.becker-hickl.com/pdf/dbspc130-2.pdf, shown as TCSPC in Figure 4), where the detected photons were collected in a series of time channels of different delays with respect to the synchronism signal sent by the laser when a pulse was
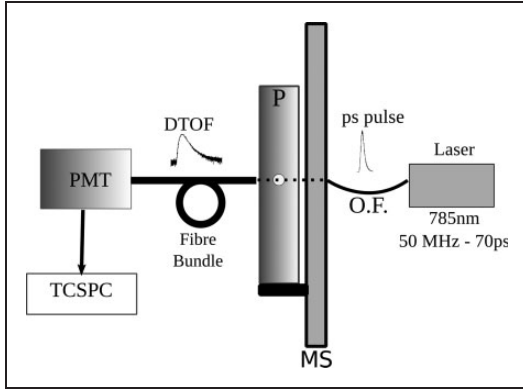
Figure 4. Set-up for *time-resolved imaging* (TR) experiments (P: Phantom, PMT: photomultiplier, TCSPC: time correlated single photon counting board, MS: movable stage).

emitted. The results are the so-called distributions of time-of-flight (DTOFs). To retrieve the optical properties of the bulk, the obtained DTOFs, which are typically a few *ns* wide, were fitted using the theoretical model proposed by Contini et al.[1] for turbid media slabs. The expression for the diffuse transmittance $T(s,\rho,t)$ per unit time and unit area, for a slab of thickness s, reduced scattering coefficient μ'_s and absorption coefficient μ_a, for a medium that fulfils the diffusion approximation, results:

$$
\begin{aligned}
&T(s, \rho, t) \\
&= \frac{\exp(-\mu_a v t - \frac{\rho^2}{4Dvt})}{2(4\pi Dv)^{3/2} t^{5/2}} \\
&\times \sum_{m=-\infty}^{\infty} \left[z_{1,m} \exp\left(\frac{-z_{1,m}^2}{4Dvt}\right) - z_{2,m} \exp\left(\frac{-z_{2,m}^2}{4Dvt}\right) \right]
\end{aligned}
\tag{3}
$$

where $D = (3\,\mu'_s + \mu_a)^{-1} \approx (3\,\mu'_s)^{-1}$ is the diffusion coefficient, $v = cn^{-1}$ is the speed of light in the medium, and $z_{1,m} = s(1-2m) - 4mz_e - z_0$, $z_{2,m} = s(1-2m) - (4m-2)z_e + z_0$. For a refractive index of $n = 1.4$, which is an approximate value for agarose with milk, the extrapolated distance z_e, where the diffuse intensity vanishes, results in $z_e \approx 2.05(\mu'_s)^{-1}$. In equation (3), ρ is the lateral offset between the source and the detector, which for this work was taken as zero in all cases. The measured DTOFs, together with the corresponding Instrument Response Function (IRF) for the experimental setup are given as inputs in a self-developed Levenberg–Marquardt routine, implemented in open source Python language (www.python.org), which in turn gives the set of optical parameters that minimises quadratic errors. Briefly, the algorithm begins with some initial values for the optical properties, constructs a curve accordingly with equation (3), convolves it with the IRF and compares the result with the experimental curve. The optical properties are automatically varied until convergence is reached.

The optical properties of the host were measured after the construction of the phantom. To this end, the fibres were properly placed, far enough from the inclusions. They were measured on different positions to check if the two steps fabrication process of the phantom negatively affected the homogeneity of the host.

Another experiment performed, aiming to study the variation of the DTOFs in several positions of detection on the phantom due to the presence of inhomogeneities, was a TR transilluminance scanning. The scanning was performed along horizontal lines in x direction. Please refer to the geometry of Figure 2. Using the same experimental set-up shown in Figure 4 and with the help of the translation stage (MS in the figure), a set of DTOFs were collected by horizontally scanning the surface of the phantom from $x = -4$ cm to $x = 4$ cm in 2 mm steps (40 measurement points). The procedure was repeated for five different heights, namely $y = -1$ cm to $y = 1$ cm step 0.5 cm. Since variations of the DTOFs curves are related to changes in the optical properties, we analysed these temporal profiles to associate their changes with the presence of the inclusions along the scanning positions. The analysis was made by dividing the DTOF's into 10 time-sections, each containing an equal number of photons, called "deciles". A reference DTOF (far from the inclusion) was used to determine the time points t_j that defined the deciles.

It is a well-established fact that, for a given DTOF, its rising edge (early photons, contained in the first decile ($t_0 \leq t < t_1$)) is more sensitive to changes in the reduced scattering coefficient, while the behaviour of its tail (photons inside the eighth decile ($t_7 \leq t < t_8$)) is dominated by the absorption coefficient.[26] The situation is sketched in Figure 5, where the first and eighth deciles are shown in a typical DTOF (Figure 5(a)) together with the most probable avarage paths for the photons in each of these deciles (Figure 5(b)). Note that the early photons follow shorter average paths, while late photons go through larger trajectories, thus spending longer time inside the medium, with the consequent increase of the absorption probability. Although this procedure did not allow a quantitative determination of the optical properties of the inhomogeneous medium containing the inclusions, it provided a useful tool to detect variations, being sensitive to increments as well as reductions in the effective optical properties resulting from the combination of those of the host with those of the inclusions. For example, an increment in the reduced scattering coefficient will retard the DTOF, thus reducing the number of photons in the first decile. On the contrary, if μ'_s decreases, the entire DTOF shifts to smaller times, increasing the number of early photons. Similar reasoning applies to the eighth decile if changes in the absorption coefficient are considered.

We also studied the behaviour of the normalised integrated intensity (*NII*) of each DTOF.
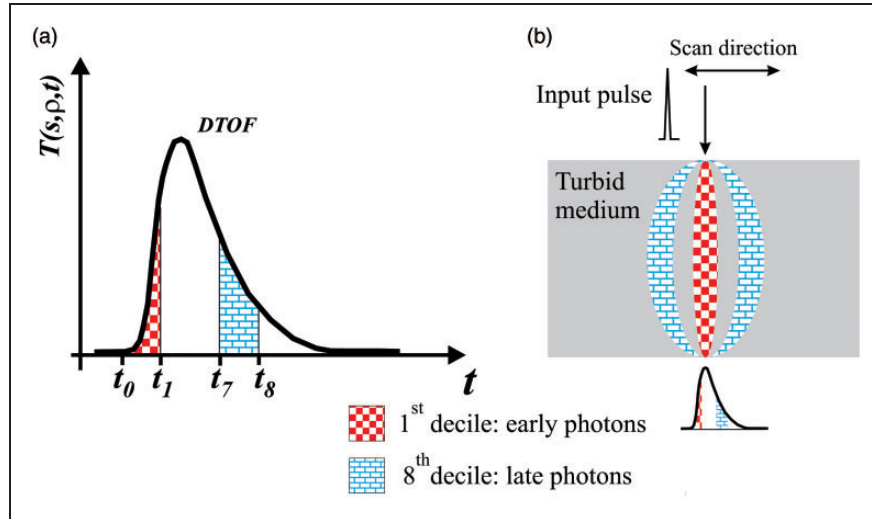
Figure 5. Scheme of a *distributions* of time of flight (DTOF) showing the construction of the deciles (a), and the most probable average paths followed by photons inside the turbid medium (b).

The normalisation reference was taken at a point far from the inclusions.

The number of photons in the first and eighth deciles, as well as the *NII* was obtained for each scanning position, and their changes were analysed in the so-called transilluminance profiles, which present the values of these three parameters as a function of the *x* position.

The change in percentage for the transilluminance profiles C_{TR} is defined as

$$C_{TR}(x) = \left[\frac{\int_0^{t_{10}} T_x(s, \rho, t)\mathrm{d}t}{\int_0^{t_{10}} T_{far}(s, \rho, t)\mathrm{d}t} - 1 \right] \times 100 \qquad (4)$$

where the subscript x denotes the DTOF for the corresponding x position and $T_{far}(s, \rho, t)$ is the transmittance profile acquired far from the inclusions; the information achievable from the *NII* results is comparable to the CW measurements already described.

Results and discussion

We present here the discussion of the main results obtained for the characterisation of the phantoms of Table 1, accordingly to both methods described previously.

CW experiments: transmittance images

In Figure 6, we present the normalised images for the centre position $(x, y) = (0, 0)$ of each phantom, and the corresponding contrast profiles along the x direction and at the vertical coordinate y where the nominal location of the inclusion occurs accordingly with Table 1. For example, the image at the top left corner corresponds to phantom P1, for which, as shown in Table 1, a Type (*A*) inclusion was located at $(x, y, z) = (-0.3,$

$-0.3,$ 0) cm. The horizontal profile is thus drawn at $y = -0.3$ cm.

In all cases shown, the presence of the inclusions, either absorbing or not, and their relative absorption with respect to the host can be assessed. It is important to mention that using this analysis, it was not possible to determine the optical properties of the inclusion itself, but it detected the effective absorption variation of the whole medium (host and inhomogeneities). The positions of the extremes (maxima or minima) visible in the contrast profiles matched with fairly good agreement the actual positions of the inclusions in the respective phantom, as indicated in Table 1. The shifts of the spots representing the inclusions were due to the fact that they were not positioned on the optical axis of the source-camera system.

Looking at the contrast profiles vs. x in Figure 6, plotted in the centre-y position of the controlled inhomogeneities, shown below the corresponding image, it was possible to distinguish the difference in values for the different types and sizes of inhomogeneities. Looking at P1 and P2 contrast C_{CW}, given by equation (2), the maximum value for the first case was 40%, while for the second it was 20%, which is consistent with the fact that P1 contained a non-scattering inhomogeneity, type (*A*), compared to the non-scattering in P2, type (*B*). Evaluating the images obtained for P3, P4 and P5, the presence of the two non-scattering inclusions, type (*A*), can be distinguished. The contrast for the smaller inclusions, with a diameter of 0.6 cm, contained in P4 and P5, was up to 20% smaller compared to the contrast of the inclusions of 1 cm of diameter contained in the same phantoms. Taking into account Figure 5(b), this reduction in contrast can be explained because for a smaller inclusion there is a lower volume of the photon paths that is affected by the presence of the inclusion. Consistently with this previous statement, for the case of P3, with two inhomogeneities of the same sizes and the same optical
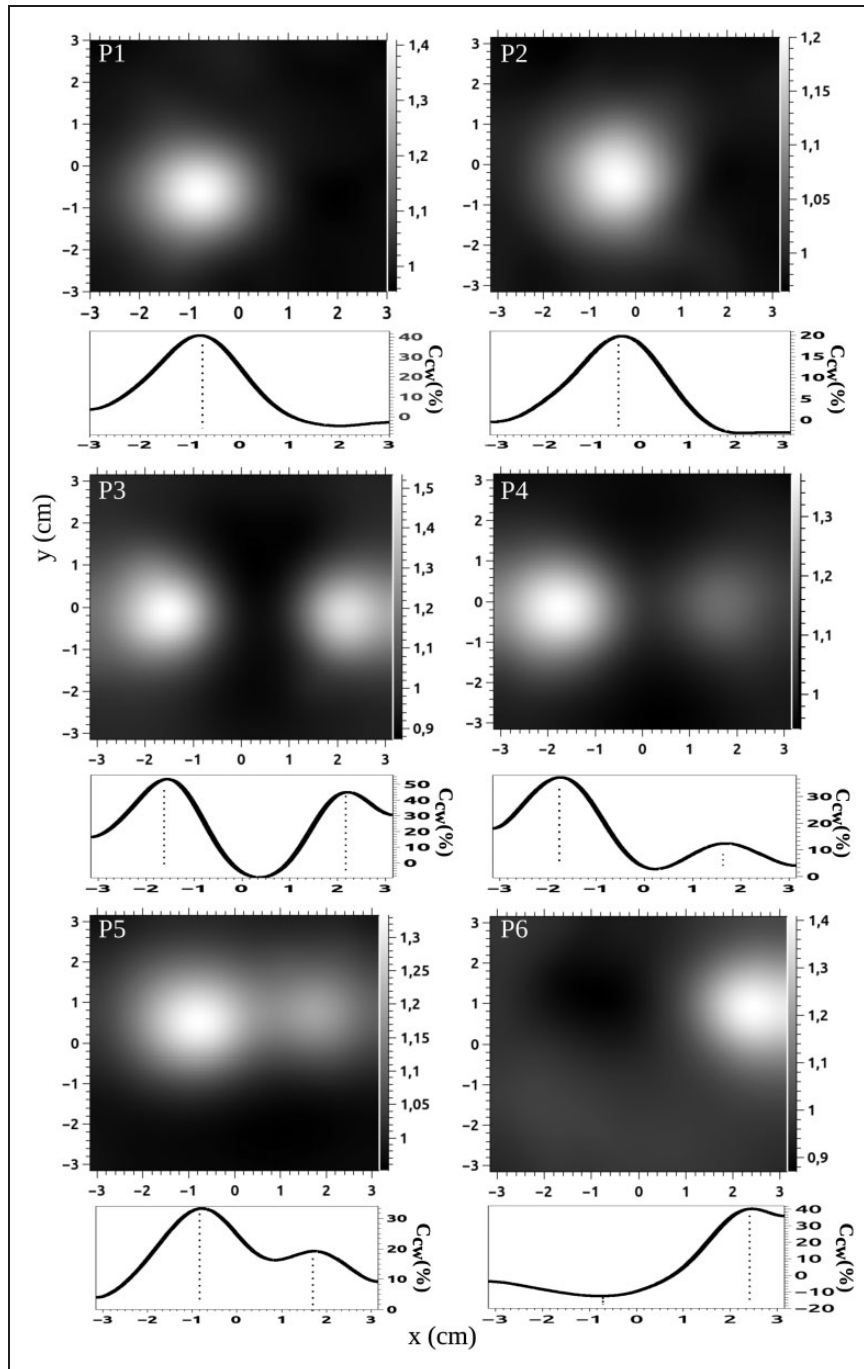
Figure 6. Centre images after dividing them by the background. Additionally, the percentage contrast profiles centred at the diameter of the inclusions.

properties, the contrast due to each of them is almost equal.

Finally, with reference to the last picture in Figure 6, the presence of the high-scattering and double absorption inclusion, type (*C*), on the left side in P6 can be assessed, even in the presence of the high contrast due to the non-scattering inclusion, type (*A*), on the right side of P6. The negative contrast value for the first one was −12%, indicating the absorbing nature of this inclusion, while for the inclusion on the right, the contrast value was +40% due to the low-absorbing and

non-scattering nature of it, relative to the host. Note that this value for the positive contrast is of the order of the other contrasts found for all the cases of these types (*A*) of inclusions of 1 cm diameter.

Considering the MC simulation, in Figure 7 there is presented the centre image for the phantom P1, with the inclusion in the position and with dimensions indicated in Table 1. The normalisation was performed by dividing the image obtained for the simulation with the inclusion in the medium by the background simulated image, without inclusion. Comparing it to the

experimental image, the position and value of the maximum contrast showed very good agreement, since the value of C_{CW} matched with the experimental value of 40% according to equation (2) and the position was shifted from the actual position in 0.2 cm to the left, which was lower than the experimental shift of 0.4 cm. As an independent evaluation, the MC result validated the experimental procedure and the results obtained for this kind of phantom.

TR experiments: bulk optical properties and transilluminance profiles

As a first basic characterisation of the phantoms, we investigated the homogeneity of the agarose host. To this end, we used the theoretical model proposed by Contini et al.[1] accordingly to equation (3) to fit the DTOFs measured at four different positions far from the known location of the inclusions. The resulting average optical properties are shown in Table 2 together with the four individual measurements for each case. The good homogeneity and low dispersion
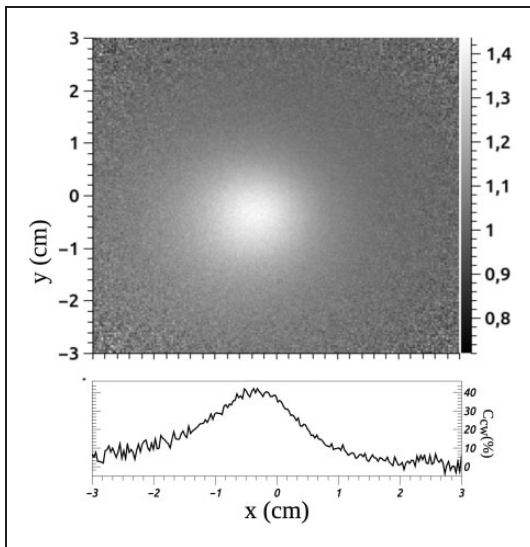
of the average values for each phantom validated the elaboration process, indicating that there was no significant alteration of the homogeneous agarose host if it was constructed in two steps as proposed (see Section *Phantom fabrication*). The reproducibility of the optical properties for the host phantom was within 10%, which is a typical value for agarose preparations.[26]

In Figure 8 we present the change in percentage for the transilluminance profiles along the x direction in 2 mm steps and at the height corresponding to the centre of the inclusions. As mentioned in the previous section describing the methods of characterisation, from the DTOFs obtained for each point, we analysed the variations of the *NII*, defined above, and the first and eighth deciles (1stD and 8thD) vs. x. Thus, in the figure there are plotted three symbols for each position of the optical fiber. The percentage changes defined by equation (4) are presented in the figure as follows: the black dots represent the *NII*, the blue star is the normalised total number of photons inside the first decile, and the hollow red triangles represent the normalised number of photons in the eighth decile. The scales of the graphics were properly selected for each case, in order to obtain the best visualisation.

In general, from the comparison of the parameters presented in Figure 8, it can be assessed that the 1stD gave the highest variation, thus indicating that it was the most sensitive to the relative scattering changes. Phantom P5 was a good example, since it included two inhomogeneities close to each other, and the 1stD clearly defined them, better than the *NII*, while the 8thD decile failed to resolve them.

Analysing the percentage change of the transilluminance profiles in Figure 8, comparing phantoms P1 and P2, both containing one inclusion of the same size, but the first with non-scattering, type (*A*), and the second one with low-scattering characteristics, type (*B*), the maximum values found were noticeably higher for the first phantom. Accordingly, to equation (4), P1 presents a *NII* 35% higher than P2; consistently the value of the 8thD was 10% larger than the one for P2, and the value of 1stD was 70% larger. The 1stD presents the highest change, consistent with a higher

Figure 7. Normalised image obtained from Monte Carlo (MC) simulation performed for P1.

Table 2. Optical properties of the host, for each phantom, obtained by fitting the *distributions of time of flight* (DTOF) taken in the four positions (x, y) indicated, and the corresponding average value and standard deviation.

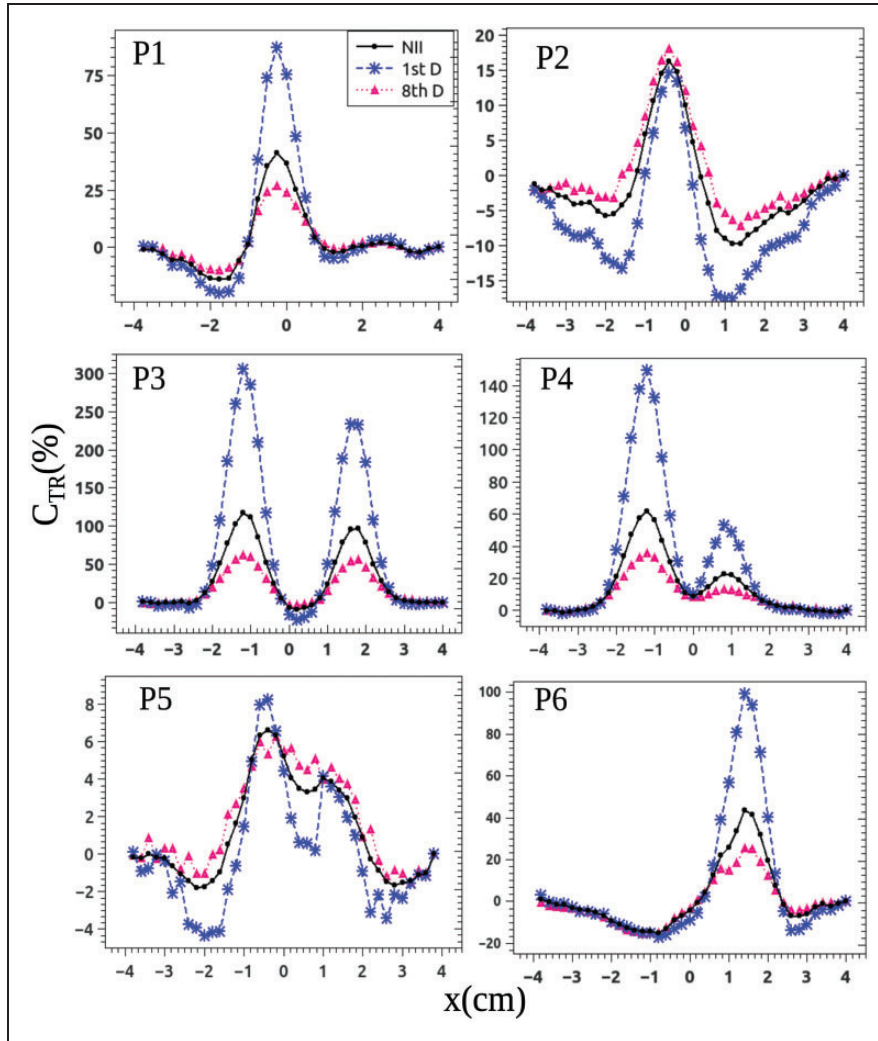| (x, y)	(5 cm; 5 cm)		(5 cm; −5 cm)		(−5 cm; 5 cm)		(−5 cm; −5 cm)		Average	
Phantom	μ'_s (cm^{-1})	μ_a (cm^{-1})	μ'_s (cm^{-1})	μ_a (cm^{-1})	μ'_s (cm^{-1})	μ_a (cm^{-1})	μ'_s (cm^{-1})	μ_a (cm^{-1})	μ_{a0} (cm^{-1})	μ'_{s0} (cm^{-1})
P1			8.61	0.098	8.34	0.091			0.09 ± 0.01	8.6 ±
P2	6.89	0.091	6.71	0.090	6.79	0.091	6.89	0.091	0.09 ±	6.8 ±
P3			8.86	0.091	8.63	0.092			0.09 ±	8.7 ±
P4	8.81	0.083	8.75	0.084	8.11	0.082	8.93	0.085	0.08 ±	8.7 ±
P5	7.43	0.089	7.67	0.087	7.45	0.086	7.56	0.086	0.08 ±	7.6 ±
P6			8.17	0.090	8.73	0.092			0.09 ±	8.5 ±

Figure 8. Results for *time resolved imaging* (TR) experiments. In all cases, the percentage change in the profiles corresponding to *NII*, and to the number of photons in the first and eighth deciles is presented. Normalisation is performed relative to their values far from the inclusions. The scales have been properly extended to have a better visualisation.

relative change on the scattering properties of the whole phantom.

Observing the profiles obtained for P3 and P4, both containing non-scattering inclusions of different sizes, the values for the integrals presented much lower maximum values for P4, for the three analysed parameters. This can be ascribed to the fact that P4 contained an inclusion with half of the diameter, producing a smaller local reduction in the relative scattering and absorption coefficients.

Finally, the analysis of the percentage change of the transilluminace profile corresponding to phantom P6 presented the maximum value corresponding to the non-scattering inhomogeneity, showing that the most important change on 1stD corresponding to a larger change for the relative scattering. The percentage profile also showed a region with values lower than those at the position of the inclusion with double absorption, showing both deciles and the *NII* had the same approximate change. Note that these variations were not as pronounced as the ones due to the non-scattering

inclusions. This can be explained because of the fact that the relative absorption change was only of a factor of two relative to the host, while for the case of non-scattering inhomogeneities, this change on the relative scattering coefficient was much higher.

As mentioned in the previous section, the contrast profiles obtained from CW images (Figure 6), given by equation (2), provided information equivalent to the *NII* transilluminance profiles (Figure 8, black spot). Concerning the ability of the TR approach to properly locate the lateral positions of the inclusions, we have represented in Table 3 the shifts Δx of the extreme positions from the actual x position (presented in Table 1), and the corresponding maximum values obtained from the contrast profiles obtained by CW imaging and transilluminance profiles in the TR approach. Note that the shifts for the TR results were $|\Delta x| \leq 0.15$ cm, that is smaller than the scanning step size of 2 mm., thus confirming the ability of properly localised inhomogeneities of this approach. The shift on the CW was due to the fact that the emitting fibre was

Table 3. Comparison of contrast values obtained for the contrast profiles in continuous wave transmittance (CW) with the transilluminance profiles obtained in time-resolved imaging (TR).

	Inclusion #1				Inclusion #2			
	Δx(cm)		Extreme value		Δx(cm)		Extreme value	
Phantom	CW	TR	C_{CW}	C_{TR}	CW	TR	C_{CW}	C_{TR}
P1	−0.45	0.00	41%	41%				
P2	−0.40	−0.05	20%	16%				
P3	−0.35	+0.05	53%	116%	+0.50	0.00	45%	55%
P4	−0.55	−0.05	37%	116%	+0.70	−0.15	12%	23%
P5	−0.55	−0.15	33%	6%	+0.50	−0.15	19%	4%
P6	+0.05	−0.05	−12%	−16%	+1.00	0.00	40%	43%

Note: The lateral shift relative to the actual position of the inclusions, Δx, is also given.

not located in the centre of the inclusions, while in the case of the transilluminance configuration, the emitting and detecting fibres were placed in a common axis, and moved together during the scanning. Regarding the values of the extremes, they did not match in all cases, being the most apart for each approach, CW and TR, for the cases with two non-scattering inclusions (P3, P4 and P5). This can be ascribed to noise introduced by the bigger intensity due to the non-scattering and low absorbing inclusions in the acquisition of the corresponding DTOFs, which are highly sensitive to the noise.

Conclusions

We have presented an innovative technique, using a tool from the molecular gastronomy, called inverse spherification, for the fabrication of solid phantoms, with liquid spherical inclusions for their use in biomedical optics experiments. These phantoms mimicking cystic inclusions, to our knowledge never reported before, show potential applicability and reliability for their use in the development of optical techniques for the detection of heterogeneities with very low and non-scattering and/or low absorption coefficients. They can be constructed easily, fast and at low cost, and allow realistic 3D geometries to be considered to study in transmittance configurations, with both continuous wave and time-resolved set-ups.

The constructed phantoms were characterised by measuring optical properties of the bulk, analysing the transmittance images and the corresponding contrast profiles, and studying the time-resolved transilluminance profiles. These studies show that the proposed construction technique for both, bulk and inclusion, preserves the geometry of the inclusion thus demonstrating its practical feasibility. The optical properties of the inclusion relative to the ones of the background could be determined by both the CW approach and the TR experiments. However, the actual optical properties of the inclusions cannot be retrieved since both approaches can only give information about the effective optical properties along the total thickness of the

phantoms. Besides, the lateral locations of the inclusions in the plane (x, y) can be assessed, by both kinds of experiments presented. Due to diffusion, the CW experiments produce errors in these locations of about twice the positioning step, while the TR transilluminance approach gives errors below these steps.

References

1. Contini D, Martelli F and Zaccanti G. Photon migration through a turbid slab described by a model based on diffusion approximation. I. Theory. *Appl Opt* 1997; 36: 4587–4599.
2. Yang D, Chen X, Ren S, et al. Influence investigation of a void region on modeling light propagation in a heterogeneous medium. *Appl Opt* 2013; 52: 400.
3. Bal G. Transport through diffusive and nondiffusive regions, embedded objects, and clear layers. *SIAM J Appl Math* 2000; 62: 1677–1697.
4. Farina A, et al. Multi-laboratory investigation of the optical properties of the [AQ1]human head. *Proc. SPIE* 8804, 880405-880408, 2013.
5. Arridge S, Dehghani H, Schweiger M, et al. The finite element model for the propagation of light in scattering media: a direct method for domains with nonscattering regions. *Med Phys* 2000; 27: 252–264.
6. Xu Y, Zhang Q and Jiang H. Optical image reconstruction of non-scattering and low scattering heterogeneities in turbid media based on the diffusion approximation model. *J Opt A* 2004; 6: 29–35.
7. Ripoll J, Nieto-Vesperinas M, Arridge S, et al. Boundary conditions for light propagation in diffusive media with nonscattering regions. *J Opt Soc Am* 2000; 17: 1671–1681.
8. Wróbel M, Popov A, Bykov A, et al. Multi-layered tissue head phantoms for noninvasive optical diagnostics. *J Innovat Opt Health Soc* 2014; 8: 1541005.

9. Pifferi A, et al. Mechanically switchable solid inhomogeneous phantom for performance tests in diffuse imaging and spectroscopy. *J Biomed Opt* 2015; 12: 121304.

10. Wabnitz H, et al. Performance assessment of time-domain optical brain imagers, part 1: basic instrumental performance protocol. *J Biomed Opt* 2014; 19: 086010.

11. Wabnitz H, et al. Performance assessment of time-domain optical brain imagers, part 2: nEUROPt protocol. *J Biomed Opt* 2014; 19: 086012.

12. Pardini P, Waks Serra M, Ranea-Sandoval H, et al. Study of inks used in biomedical optics phantoms. Stability and ageing. *J Near Infrared Spectrosc* 2015; 23: 219–225.

13. Di Ninni P, Martelli F and Zaccanti G. The use of India ink in tissue-simulating phantoms. *Opt Express* 2010; 18: 26854–26865.

14. Martelli F, et al. Phantoms for diffuse optical imaging based on totally absorbing objects, Part 1: basic concepts. *J Biomed Opt* 2013; 18: 66014.

15. Martelli F, et al. Phantoms for diffuse optical imaging based on totally absorbing objects, Part 2: experimental implementation. *J Biomed Opt* 2014; 19: 076011.

16. Yang D, Chen X, Peng Z, et al. Light transport in turbid media with non-scattering, low-scattering and high absorption heterogeneities based on hybrid simplified spherical harmonics with radiosity model. *Biomed Opt Express* 2013; 4: 20209.

17. Xu Y, Gu X, Fajardo L, et al. In vivo breast imaging with diffuse optical tomography based on higher-order diffusion equations. *Appl Opt* 2003; 42: 3163–3169.

18. Jiang H, Paulsen K and Osterberg U. Optical image reconstruction using DC data: simulations and experiments. *Phys Med Biol* 1996; 41: 1483–1498.

19. Cucher MA, et al. Cystic echinococcosis in South America: systematic review of species and genotypes of *Echinococcus granulosus* sensu lato in humans and natural domestic hosts. *Trop Med Int Health* 2015; 21: 166–175.

20. http://www.amazingfoodmadeeasy.com/info/modernist-techniques/more/spherification-technique. [AQ2]

21. Vo-Dinh T (ed.). *Biomedical photonics handbook*. Boca Raton, FL: CRC Press, 2003.

22. Taroni P, Pifferi A, Salvagnini E, et al. Seven-wavelength time-resolved optical mammography extending beyond 1000 nm for breast collagen quantification. *Opt Express* 2009; 17: 15932–15946.

23. Carbone NA, et al. Diffuse Reflectance optical topography: location of inclusions in 3D and detectability limits. *Biomed Opt Express* 2014; 5: 1336–1354.

24. Carbone NA, Di Rocco, Iriarte D. I., O., et al. Solution of the direct problem in turbid media with inclusions using Monte Carlo simulations implemented in graphics processing units: new criterion for processing transmittance data. *J Biomed Opt* 2010; 15: 035002.

25. Ripoll J and Nieto-Vesperinas M. Index mismatch for diffuse photon density waves at both flat rough diffuse-diffuse interfaces. *J Opt Soc Am A* 1999; 16: 1947–1957.

26. Waks Serra MV, et al. Diffuse light transmission profiles obtained using CW: A comparative analysis with time resolved experiments. *Opt Int J Light Electron Opt* 2014; 125: 3507–3513.